The long-period superstructures in binary $Au_{3+x}Zn_{1-x}$ alloys: stability and off-stoichiometry effects

1990 J. Phys.: Condens. Matter 2 3459

(http://iopscience.iop.org/0953-8984/2/15/004)

J. Phys.: Condens. Matter **2** (1990) 3459–3477. Printed in the UK

The long-period superstructures in binary $Au_{3+x}Zn_{1-x}$ alloys: stability and off-stoichiometry effects

D Broddin, G Van Tendeloo and S Amelinckx
University of Antwerp, RUCA, Groenenborgerlaan 171, B-2020 Antwerpen, Belgium

Received 30 October 1989

Abstract. A detailed analysis by means of high-resolution electron microscopy (HREM) of the long-period anti-phase boundary structures in $Au_{3+x}Zn_{1-x}$ alloys is presented. The initial complex one-dimensional superstructures, consisting of a uniform mixture of anti-phase domains of two and three $L1_2$ unit cells width, are found to be metastable. Comparison between observed and calculated HREM images along two distinct zone axes indicates that the anomalous contrast in the imaging of the minority ⟨3⟩ domains in the off-stoichiometric alloys can be attributed to a combined decrease of the order parameter and a localised accommodation of excess Au. Monte Carlo simulations in the context of the three-dimensional face-centred cubic Ising model are presented, which show a similar localised decrease of the order parameter and the localisation of excess Au at an isolated ⟨3⟩ wall in a ⟨2⟩ structure, the first effect being dominant at high temperatures whereas the latter effect is more important at low temperatures. The localisation of excess Au at the ⟨3⟩ walls is shown to play an important role in the decomposition process, which causes a compositional segregation after prolonged annealing, with the commensurate ⟨2⟩ structure as one of the end-products. The electron microscope observations are interpreted in terms of a possible microscopic model for the segregation mechanism.

1. Introduction

Since Johansson and Linde's (1936) discovery of long-period modulated phases in Cu–Au, the list of (noble-metal) alloy systems exhibiting long-period order has grown considerably, mainly due to the intensive research of Schubert and coworkers (Schubert *et al* 1954, 1955, Wilkens and Schubert 1958).

The beautiful regularity of the anti-phase domain sequences, postulated by Fujiwara (1957) from the analysis of (in)commensurate diffraction spectra, has led to numerous studies by means of electron imaging techniques. The principle of uniformity, which explains the anti-phase domain sequences corresponding to non-integer modulation wavelengths (in terms of the basic lattice parameter), has gained credibility to such an extent that deviating domain sequences are often considered as non-equilibrium situations as in Ag_3Mg (Kulik *et al* 1987) and Cu_3Al (Broddin *et al* 1989).

The similarity of the observed domain sequences in alloys with those arising in statistical studies of phenomenological Ising models, such as the axial next-nearest-neighbour Ising (ANNNI) model (Selke 1988), lead to new experiments where the effect of temperature on the phase stability is considered. Possible temperature effects were discussed by De Fontaine and Kulik (1985) in a general way, while more detailed

0953-8984/90/153459 + 19 $03.50

experimental studies were performed for Al_3Ti (Loiseau *et al* 1985) and Cu_3Pd (Broddin *et al* 1986, 1988c). Indications were found for lock-in phenomena favouring commensurate phases at low temperatures, while delocalisation of walls seems to govern the behaviour of incommensurate phases at high temperatures.

The Au–Zn system with its characteristic domain sequences of two or three unit cell slabs width, occurring for Au–Zn alloys with a composition around 20 at.% Zn, is often referred to as a prototype of ANNNI model-like behaviour (de Fontaine and Kulik 1985, Van Tendeloo and Amelinckx 1988). However, not very much is known about the fine structure of the phase diagram in the Au_3Zn composition region. The most detailed results were reported by Iwasaki and coworkers (Iwasaki *et al* 1960, Iwasaki 1962), who established the stability of the phase Au_3Zn (H) and its room-temperature modifications (R1) and (R2) near stoichiometry and a two-dimensional long-period structure around 17 at.% Zn. These results were accepted in the recent phase diagram compilation by Okamoto and Massalski (1989). It is concluded that Au_3Zn (H), the FCC-based long-period phase referred to in the context of the ANNNI model, consists exclusively of anti-phase domains of two unit cells width ($M = 2$, where M denotes the average number of unit cell slabs per anti-phase domain). More complex domain sequences in which domains of two and three cells width are mixed in a uniform way (according to Fujiwara's principle of uniformity), which are mainly observed in off-stoichiometric (low Zn content) alloys after relatively short annealing time periods (Van Tendeloo and Amelinckx 1977, Teuho and Mäkinen 1982), are classified as unstable in the compilation of Okamoto and Massalski (1989).

To the best of our knowledge, the observed M values in the binary system are always lower than 2.33. This upper limit can be realised by fast cooling of alloys with 18–19 at.% Zn inhibiting the formation of the 2D structure. Earlier reports of the observation of $M = 3$ (Van Tendeloo and Amelinckx, 1977, 1988) were presumably based on an erroneous interpretation of dark-field lattice fringes, where the $M = 3$ fringes were in fact the images of the non-conservative anti-phase boundaries (APB) in a variant of the 2D structure in which the conservative APB are extinct. We will show that most of these complex sequences in the binary system are eliminated after prolonged annealing and only the $M = 2$ structure can be considered as ultimately stable, in agreement with the assumptions in the phase diagram compilation, which is based on the *in situ* high-temperature electron diffraction results by Teuho and Mäkinen (1982), and which indicated a change of the initial period different from 2 towards the simple $M = 2$ structure after longer annealing.

Although the original aim of this study was to analyse the behaviour as a function of temperature of the different long-period structures (LPS) in $Au_{3+x}Zn$, most of the results presented here are concerned with the transformation mechanism and the time evolution of these (often metastable) structures and the characterisation of their anti-phase and composition modulation profiles.

2. Crystal structures

2.1. Au_3Zn (H)

This FCC superstructure with Au_3Zn stoichiometry is often denoted DO_{23} ($M = 2$). At the stoichiometric composition, it is stable between 250 and 415 °C.

2.2. $Au_{3+}Zn$ (2D)

This FCC superstructure is stable as a single phase around 17 at.% Zn below 285 °C. It is a two-dimensional anti-phase boundary structure of the Cu_3Pd type (Watanabe and Ogawa 1956, Broddin *et al* 1986) and it has been studied extensively by high-voltage high-resolution electron microscopy by Terasaki and coworkers (Terasaki and Watanabe 1981, Terasaki 1981, 1982). The accommodation of excess gold at the non-conservative anti-phase boundaries is expected to play an important role in its stabilisation.

2.3. Au_3Zn (R_1 and R_2)

These structures can be considered as being derived from the Au_3Zn (H) structure by a symmetry-lowering deformation modulation. This deformation occurs below a transformation temperature; the transformation temperatures are largest for alloys close to the stoichiometric composition (at ~24.5 and ~27 at.% respectively). Moreover, the transformation cannot be suppressed by quenching for nearly stoichiometric alloys.

2.4. LPS with $M \neq 2$

Structures like . . . 22232223. . . (further denoted $\langle 2^3 3 \rangle$) are most frequently observed around 20 at.% Zn. Often the structures are found to coexist with areas having the 2D LPS. Such coexistence observations have been interpreted as transient states during the growth or the withdrawal of the 2D LPS within the 1D LPS (with $M \neq 2$) (Van Tendeloo and Amelinckx 1977, Schrijvers *et al* 1983). The coexistence of LPS with $M \neq 2$ and the Au_3Zn (H) structure ($M = 2$) was observed at around 21 at.% Zn by Teuho *et al* (1987). The (meta)stability of LPS with $M \neq 2$ will be discussed in section 6.

3. Experimental procedure

Binary alloys with nominal compositions Au–18.5, 19.5, 20.5, 21, 22 at.% Zn were melted in evacuated quartz tubes and homogenised. The ingots were cold-rolled to foils and disc specimens were cut from these foils. The cut specimens were annealed at 550 °C for three days for stress relief. After quenching, in order to freeze in an excess vacancy concentration and to speed up the diffusion at lower temperatures, annealing for periods ranging from a few minutes to 46 days was performed at 250, 300 and 350 °C in large-inertia oil baths.

In situ high-temperature resistivity measurements were performed for the alloy Au–21 at.% Zn, allowing an estimation of the order–disorder transition temperature and the order of magnitude of the ordering-reaction time constant at this composition (Planes 1988).

The specimens were investigated by electron diffraction and high-resolution electron microscopy (HREM) (200 and 400 kV).

4. Characterisation of the long-period structures with $M \neq 2$

4.1. HREM observations along [010]

4.1.1. Wall delocalisation. The [010] zone axis orientation is the most appropriate and most commonly used for a study of the anti-phase boundary modulation in this type of

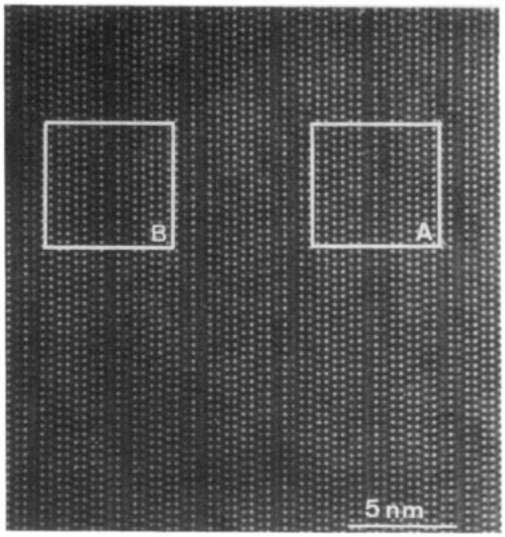

Figure 1. [0 1 0] HREM image for an Au–20.5 at.% Zn alloy taken at 400 kV. Bright dots indicate the (approximate) minority-atom columns. Note the fluctuations in the position of the ⟨3⟩ walls. Two different symmetric configurations are indicated in the regions labelled A and B.

FCC-based long-period structure. Electron diffraction patterns along this zone axis allow the M value to be determined by measuring the splitting of the high-intensity satellites around (1 0 0) along the (1 0 l) line. Imaging of the minority-atom column configuration is possible by HREM and this possibility can be related to the validity of the atom column approximation (Van Dyck *et al* 1989).

Figure 1 shows a [0 1 0] image corresponding to an Au–20.5 at.% Zn alloy annealed at 250 °C. Numerical image simulations confirmed the interpretation of the bright dot configuration in terms of the Zn-atom column configurations. (We do not incorporate minor lattice relaxations and impurity distributions at the present stage.) ⟨3⟩ domains are more or less regularly spaced (in agreement with the principle of uniformity), but the position of the ⟨3⟩ band seems to vary locally. This observation is in a sense similar to the wall delocalisation observed in Cu_3Pd and CuAuII (Broddin *et al* 1986, Van Tendeloo *et al* 1986). Like in these systems the 'fluctuations' in the wall position are connected with local shifts of the modulating function. The ⟨3⟩ domain in the . . . 22232223. . . (⟨2^33⟩) structures of $Au_{3+x}Zn$ can be considered as a 'wall', using the terminology of Fisher and Szpilka (1987) or as a 'soliton' using the terminology of Bak and von Boehm (1979, 1980) (both references are concerned with the statistics of the ANNNI model). The situations indicated A and B in figure 1 can be considered as limiting cases where the soliton is symmetric with respect to different crystallographic positions as indicated in figure 2. In figure 2(c) the centre of the soliton coincides with the centre of a domain, whereas in figure 2(d) the soliton is centred in between two domains. (Note that we apply the soliton terminology for analogy purposes only; additional image simulations indicate that the experimental obvservations do not agree with the detailed occupation probabilities deduced from the soliton profiles in figure 2.) The excitation-like character of the delocalised ⟨3⟩ walls naturally leads to broad (weakly pinned) solitons. More common in the case of long-period structures, but essentially equivalent, is the description in terms of a smoothing of the modulation profile, i.e. the discontinuous step function of Fujiwara is smoothed as in Cu_3Pd and Al_3Ti at high temperatures (Broddin *et al* 1988c, Loiseau *et al* 1985).

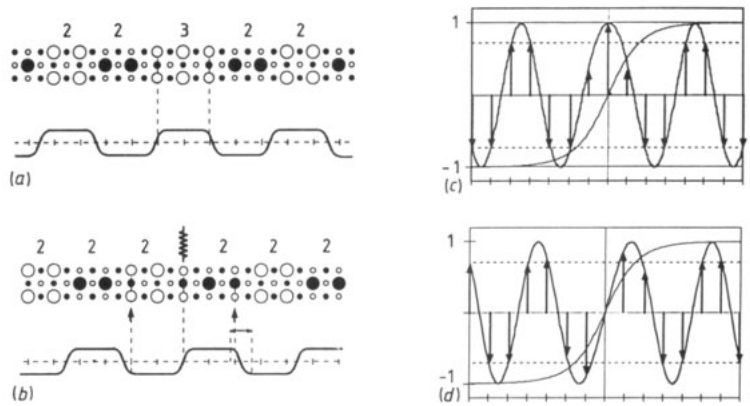

Figure 2. (*a*, *b*) Smooth profile and (*c*, *d*) soliton representation, which lead to occupation probabilities that explain the configurations in figure 1, labelled A and B respectively. The size of the circles in (*a*) and (*b*) is proportional to the Zn content in the considered columns.

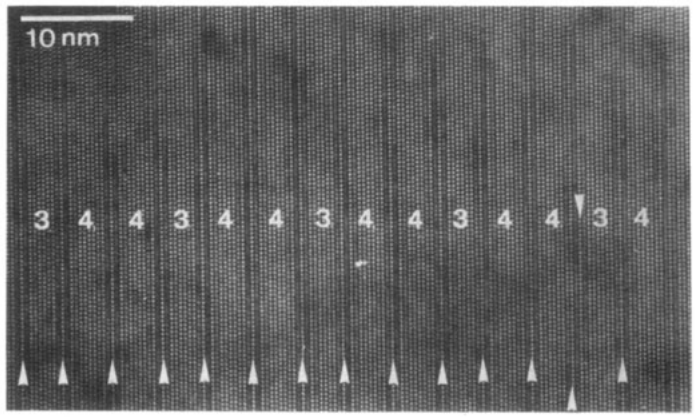

Figure 3. 400 kV [0 1 0] HREM image for an Au–20.5 at.% Zn alloy annealed at 250 °C. The domain sequence corresponds to $\langle(2^43)^22^33\rangle$. The number of consecutive ⟨2⟩ domains in between the ⟨3⟩ walls is indicated. Note the 'ledging' of a ⟨3⟩ wall at the right of the image (in between the arrows).

The anti-phase domain sequence is indicated in figure 3 in order to emphasise that the principle of uniformity remains valid for rather complex domain sequences. By counting the number of $L1_2$ unit cell slabs and the number of anti-phase domains for the area imaged in figure 3, the M value was determined to be 2.2143. The method of Fujiwara or methods like the continued fraction algorithm (de Fontaine and Kulik 1985) allow one to determine the ideal domain sequence corresponding to this M value as $\langle(2^43)^2(2^33)\rangle$, which is (apart from a phase-factor shift of the origin) the indicated sequence in figure 3. (The number of consecutive ⟨2⟩ domains in between the ⟨3⟩ domains is indicated.)

4.1.2. The change of M with the valence-electron concentration. In agreement with the predictions of Sato and Toth's model (Sato and Toth 1961, 1962a, b, 1965, 1968), in which the modulation period is related to the number of valence electrons per atom, the

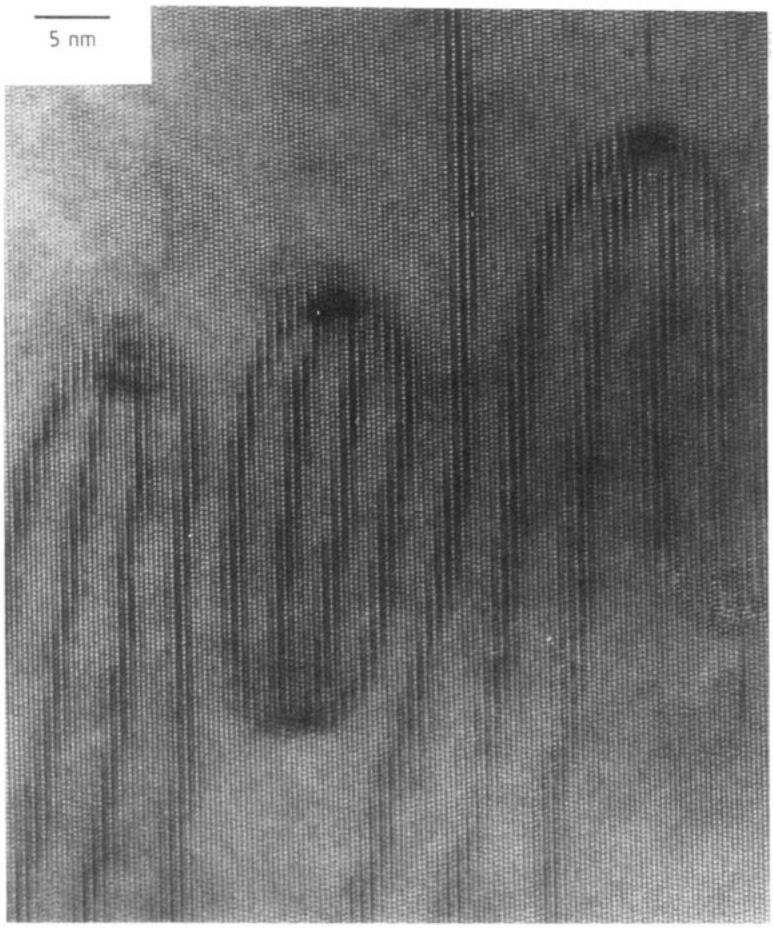

Figure 4. 200 kV [010] image for an Au–21 at.% Zn alloy annealed at 250 °C for 15 min. Note the presence of fourfold nodes of ⟨3⟩ domains, often called 'jelly-fish patterns'. The initial configuration with $M \neq 2$ is disappearing in favour of the $M = 2$ structure.

M value observed in short-time annealed binary and ternary alloys with Zn contents ranging from 15 to 22 at.% Zn decreases with increasing Zn content. The density of ⟨3⟩ walls is found to decrease with increasing Zn content until it reaches a limit at around 21 at.% Zn, where the $M = 2$ structure is formed. At low Zn content, $M = 2.33$ seems to be the uppermost value for binary alloys since the 2D structure is formed in alloys with this composition. However, the formation of the 2D structure can be suppressed by the addition of Cu (results on the influence of Cu additions will be presented in a forthcoming paper).

Especially interesting, with respect to the analogy with soliton or discommensuration pictures, are the junctions of four ⟨3⟩ walls that can be observed in the Au–21 at.% Zn alloys where the $M = 2$ structure coexists with an $M \neq 2$ phase. A HREM observation (200 kV) for such an initial configuration of coexistence is shown in figure 4. A ⟨3⟩ wall in an $M = 2$ structure can be considered as an APB with $R = -\frac{1}{4}[221]$ (or $\frac{1}{4}[001]$,

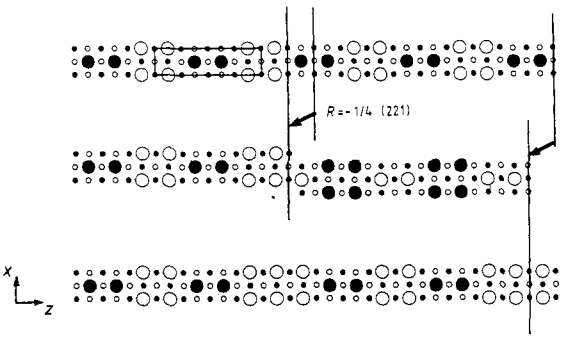

Figure 5. ⟨3⟩ domains in the $M = 2$ structure can be considered as anti-phase boundaries (APB) with displacement vector $\boldsymbol{R} = -\frac{1}{4}[221]$ in terms of the $M = 2$ unit cell. Since the total displacement after four of these APB corresponds to a lattice vector, these APB merge or annihilate in groups of four, as observed in figure 4.

since $-\frac{1}{4}[221]$ and $\frac{1}{4}[001]$ differ by $\frac{1}{2}[111]$, i.e. a lattice vector). This is shown explicitly in figure 5. Because of the factor 1/4, four of these ⟨3⟩ walls can join in one node and annihilate, thereby nucleating the $M = 2$ structure. These configurations, observed earlier by Teuho and coworkers in Au_3Zn (Teuho 1983, Teuho *et al* 1987), are non-equilibrium situations, as will be discussed in section 6. Similar junctions can be observed in the Au–20 at.% Zn alloys where they give rise to a local change in the density of ⟨3⟩ walls within an LPS with $M \neq 2$ (Broddin *et al* 1988a, b). The migration of such nodes is expected to play an important role in compositional segregation in these alloys.

4.2. HREM observations along [1 1 0]

If the anti-phase domain modulation were pure, i.e. according to a square-wave or smooth profile without any accompanying effective composition modulation, no effect of the anti-phase boundary modulation would be expected in images and diffraction patterns along the [1 1 0] zone axis orientation. This is a consequence of the fact that such a pure anti-phase boundary modulation does not affect the composition of the (0 0 1) layers (pure Au layers alternating with mixed 50% Zn–50% Au layers) while the anti-phase boundaries are invisible since their displacement vector is parallel to the viewing direction. It should not reveal any effect of the geometrical modulation; secondary effects of a displacive relaxation near the anti-phase boundaries may play a minor role. This is at variance with the experimental observations in figure 6, which corresponds to an Au–20.5 at.% Zn alloy annealed at 250 °C. Although the effect is very weak in the image of figure 6(*a*), which corresponds to a very thin crystal region (the effect is more important in thicker crystal regions), the extra modulation is clearly present. Anomalies that presumably correspond to the ⟨3⟩ domains are indicated in the lower part of figure 6(*a*) (thicker region) while the (logarithmic) power spectrum plot of figure 6(*b*), which was obtained numerically after digitisation of the region in figure 6(*a*), shows satellites corresponding to the extra modulation. The peak representation in figure 6(*c*) corresponds to a horizontal trace along the $00l$ line through the origin of figure 6(*b*), which was included in order to emphasise the extra modulation satellites. A relaxation displacement at the anti-phase boundaries would equally affect the APB between the ⟨2⟩ domains, and cannot explain the selective imaging of the ⟨3⟩ walls in the absence of other (compositional) effects.

4.3. Profile smoothing and composition effects: numerical simulations

In order to analyse the effects of a slight smoothing of the modulation profile and a possible additional composition modulation (local deficiency of Au at the ⟨3⟩ wall),

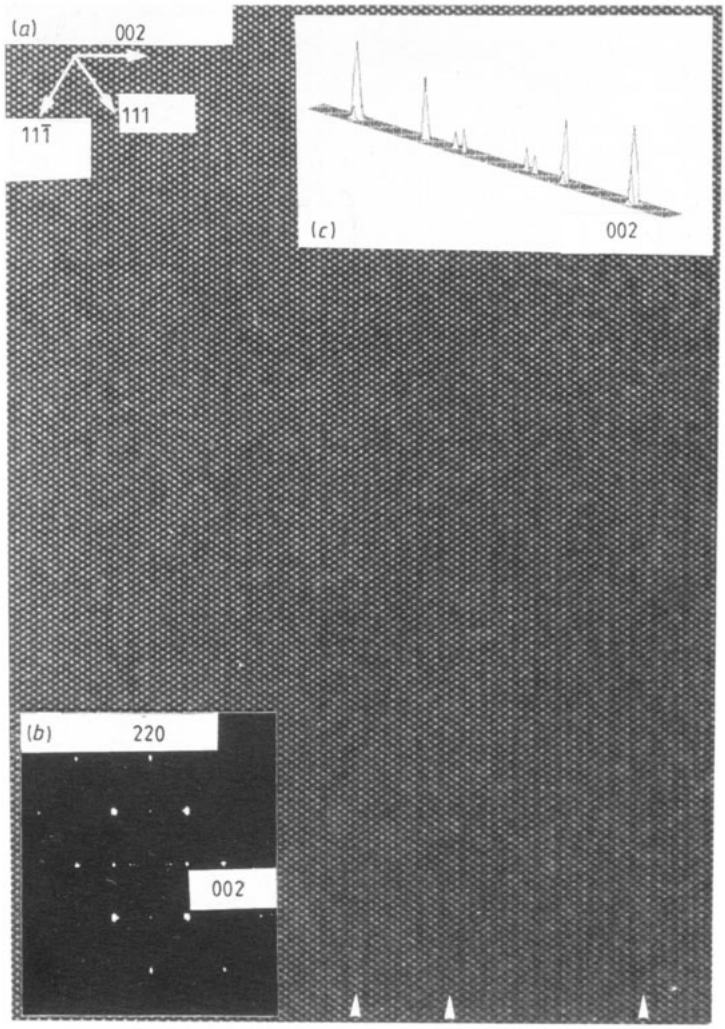

Figure 6. (*a*) 200 kV [1 1 0] HREM image for a relatively thin area in an Au–20.5 at.% Zn alloy annealed at 250 °C. Although the dot pattern corresponding to the basic lattice is predominant, a very faint extra modulation is visible in the thicker parts (⟨3⟩ walls are indicated by arrows). (*b*) A logarithmic power spectrum for the area shown in (*a*) (digitised). A peak representation for the central row in (*b*) is shown in (*c*) in order to emphasise the extra modulation satellites.

numerical simulations of the images along [0 1 0] and [1 1 0] (200 kV, C_s = 1.2 mm) were performed for three different models (figures 7 and 8):

Model a. The perfect model according to Fujiwara's principle for an LPS with M = 2.25, consisting of three consecutive ⟨2⟩ domains and one ⟨3⟩ domain (denoted $\langle 2^3 3 \rangle$). All the atom columns are either pure Au or pure Zn. The model and its derivation from a periodic step function are represented in figure 7(*a*)).

Model b. A model resulting from a slight smoothing of the modulation profile. If the smoothing is not too large, only the columns in the mixed AuZn layers at the edges of

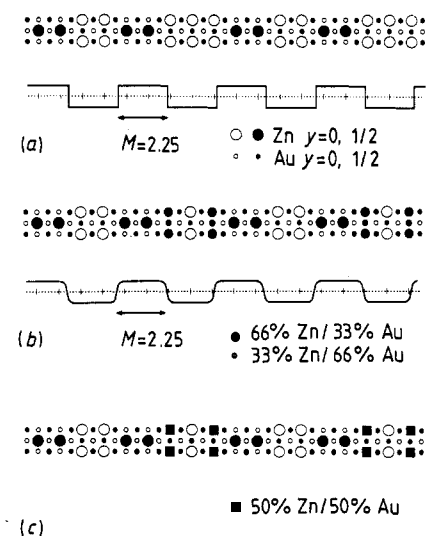

Figure 7. Structure projections along [0 1 0] for three different structure models: (*a*) square-wave modulation, (*b*) smooth profile modulation, (*c*) modulation where part of the off-stoichiometry is accommodated at the ⟨3⟩ walls.

the three domains 'feel' the smoothing: the modulation has a value different from +1 or −1 at these layers. In the present model dominant Zn columns in these layers contain 33% Au whereas the dominant Au columns in these layers contain 33% Zn. The mixed character of these columns is a result of an uncertainty in the positions of the anti-phase boundaries. Note that since Au and Zn columns are symmetrically affected, there is no net composition change for these layers as a whole (model in figure 7(*b*)).

Model c. A model in which a part of the excess gold (with respect to the stoichiometry, 25 at.% Zn) is accommodated at the ⟨3⟩ domains. A fraction (50 at.%) of the Zn in the Zn-atom columns at the edges of the ⟨3⟩ domains is substituted by Au. The nominal composition for this model is 21.53%, which is still higher than the 19.5–20.5 at.% Zn of the alloys for which the structure is most frequently observed (model figure 7(*c*)).

Especially for [0 1 0] images at intermediate to large specimen thicknesses (5–15 nm) and around Scherzer focus (−60 to −80 nm) a bright dot pattern is obtained that roughly coincides with the Zn-atom column configuration. Whereas model a reveals the domain sequence without any distinctive features, the image is clearly affected by the modifications of models b and c. At least for some of the thicknesses and defoci, low-intensity (dark) diffuse lines can be observed in figure 8 at the edges of the ⟨3⟩ domains where (part of the) atom columns are of mixed type (defocus −80 nm). Similar effects are observed in the experimental images as shown in figure 1. Although the delocalised character of the ⟨3⟩ walls clearly supports model b, the [0 1 0] images do not allow conclusions to be drawn about the validity of either model b or c, or a combination of both models.

Figure 9 shows a HREM image along [1 1 0] for a relatively thick region of the same alloy as in figure 6. An extra modulation shows up, which can be compared with the simulated images along the same zone axis for model c in figure 10. As expected, a pure anti-phase domain modulation as in model b (figure 7) does not affect the [1 1 0] image. This can be concluded from the simulated images of figure 10. The decrease in the intensity of the bright dots corresponding to the mixed 50% Au–50% Zn columns at the

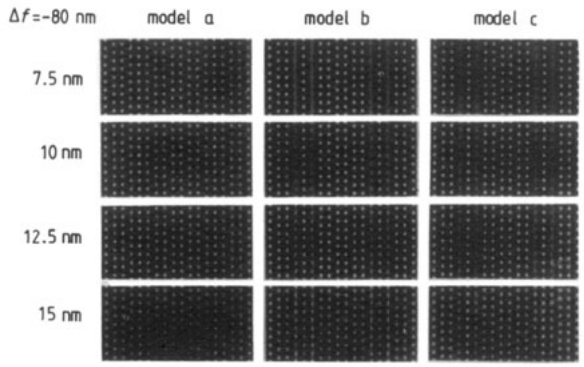

Figure 8. Simulated images for 200 kV, $C_s = 1.2$ mm, $\Delta f = -80$ nm and different thicknesses around 10 nm for the three models represented in figure 7.

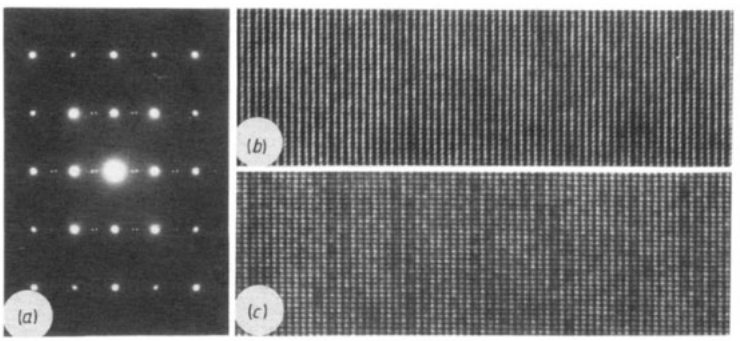

Figure 9. (*a*) Electron diffraction pattern and (*b*, *c*) 200 kV HREM images along [1 1 0] at different defocus values for a relatively thick region in an Au–20.5 at.% Zn alloy annealed at 250 °C. By comparison with the simulated images in figure 10, the defoci are estimated to correspond to −100 and −60 nm in (*b*) and (*c*) respectively.

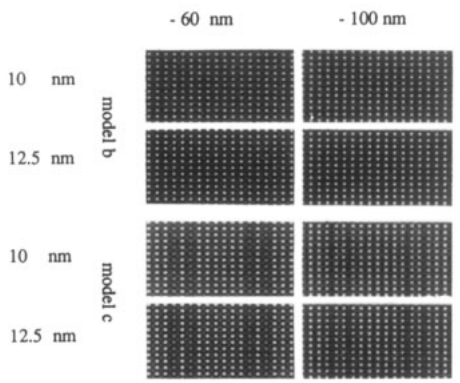

Figure 10. Simulated images along [1 1 0] (200 kV, $C_s = 1.2$ mm) for models b and c. Note the reasonable agreement between models c and b and the simulation for a defocus of −60 and −80 nm respectively.

edge of the ⟨3⟩ domains may therefore be associated with the local accommodation of a part of the Au excess with respect to the stoichiometric composition.

It is very probable that a more accurate description of the real situation would consist of a combination of models b and c. The main result of this analysis is the evidence for a composition modulation that accompanies the APB modulation. The preferential

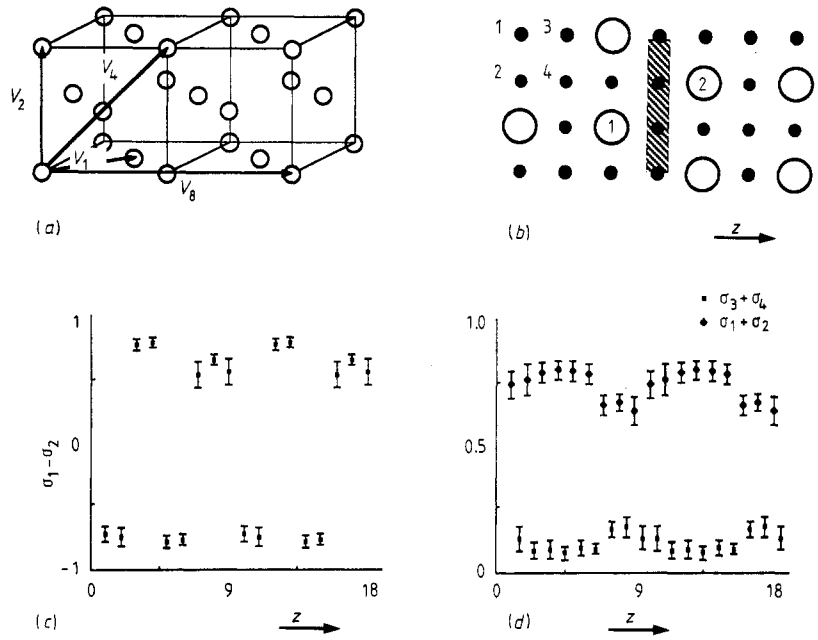

Figure 11. (*a*) Schematic drawing of the range of the interactions V_1, V_2, V_4 and V_8. (*b*) Notation of the sublattices 1, 2, 3, 4, which were used to define the sublattice occupation parameters, used in figures 12(*c*) and (*d*). (*c*) Variation of $\sigma_1 - \sigma_2$ along the modulation direction, averaged along the remaining two directions and 100 configurations (10 attempts for interchange of each site between each two configurations). (*d*) Variation of $\sigma_1 + \sigma_2$ and $\sigma_3 + \sigma_4$ along the modulation direction (same conditions as in (*c*)). Note the decrease of $\sigma_1 + \sigma_2$ at the ⟨3⟩ wall and its edges and the accompanying increase of $\sigma_3 + \sigma_4$, which is indicative of combined order-parameter and composition modulations. Error bars correspond to the standard deviation on the configuration averages.

accommodation of excess Au at the ⟨3⟩ domains is a significant result, with respect to the decomposition mechanisms presented in section 6.

5. Monte Carlo study on a 3D FCC Ising model of stoichiometry effects in ⟨2^k3⟩-type long-period structures

5.1. The model

A three-dimensional box of $M \times M \times N$ (M arbitrary, $N = 2k + 3$, k odd) conventional FCC cells (containing $4M^2N$ lattice sites) with periodic boundary conditions was filled with A and B atoms on the lattice sites. A stoichiometric (75% A, 25% B) and a non-stoichiometric (79% A, 21% B) case were considered. The initial configuration was chosen to correspond to the ideal model of figure 7(*a*) in the stoichiometric case, while in the non-stoichiometric case the excess A atoms were distributed at random over the B sites.

Following the analysis of Kulik *et al* (1987), four interactions were taken into account in order to stabilise the basic ⟨2⟩ structure: V_1, V_2, V_4 and V_8. The interaction ranges are indicated in figure 11(*a*). A classical Metropolis algorithm was used in which the system

is allowed to evolve towards an equilibrium by considering the possible interchanging of two randomly chosen A and B atoms.

The temperature was gradually increased from below and occupation averages were accumulated for the different temperatures up to the order–disorder transformation. The presence of the $\langle 3 \rangle$ domain is induced by the special value of N and the periodic boundary conditions. An analysis of the intrinsic stability domain of the $\langle 2^k 3 \rangle$ structures in a specific temperature range and for a set of V_1, V_2, V_4 and V_8 was considered to be beyond the scope of the present study. (Such an analysis in the context of the mapping of the (anisotropic) ANNNI model on an FCC Ising model with isotropic interactions (Kulik *et al* 1987) would require very high numerical precision and a quite elaborate systematic search in the (4 + 1)-dimensional parameter space.)

5.2. Results from the model

In the one-dimensional description, the occupation parameters for the four sites in the conventional FCC cell are a function of z (the modulation direction). The occupation parameters are defined as $\sigma_i = 1$ when site i is occupied with a minority atom; $\sigma_i = 0$ when this site is not occupied with a minority atom; while the site indexing is indicated in figure 11(b). The $\langle \sigma_i(z) \rangle$ parameters are averaged over the two remaining directions and over several hundred configurations. (Corrections were built in to compensate for a possible motion along z of the domain walls.)

Since σ_1 and σ_2 refer to sites 1 and 2 within the mixed planes (along the modulation direction), which accommodate in turn the minority (Zn) atoms, and σ_3 and σ_4 on the other hand correspond to sites occupied by majority atoms (Au), two combinations of these parameters were thought to be of interest:

(i) The difference $\langle \sigma_1(z) \rangle - \langle \sigma_2(z) \rangle$ describes in fact the modulating function, and changes sign when it crosses an APB. This type of profile for the non-stoichiometric case at a temperature of $T/T_c = 0.85$ is shown in figure 11(c). This profile is found to be a perfect square wave at low temperatures, especially in the stoichiometric case; while it becomes smooth and approaches a sinusoidal curve when T_c is approached.

(ii) The sums $\langle \sigma_1(z) \rangle + \langle \sigma_2(z) \rangle$ and $\langle \sigma_3(z) \rangle + \langle \sigma_4(z) \rangle$ are related to possible composition and order-parameter modulations accompanying the APB modulation, where $[\langle \sigma_1(z) \rangle + \langle \sigma_2(z) \rangle] - [\langle \sigma_3(z) \rangle + \langle \sigma_4(z) \rangle]$ can be considered as a z-dependent 'order parameter'. Especially at low temperatures, composition modulations were found to play an important role in the non-stoichiometric case: excess majority atoms are found to concentrate at the $\langle 3 \rangle$ wall. At elevated temperatures, a so-called 'order parameter modulation' is clearly established in both stoichiometric and non-stoichiometric cases. This is shown in figure 11(d) where the z dependence of $\langle \sigma_1(z) \rangle + \langle \sigma_2(z) \rangle$ and $\langle \sigma_3(z) \rangle + \langle \sigma_4(z) \rangle$ is represented for the same run as in figure 11(c). The decrease of $\langle \sigma_1(z) \rangle + \langle \sigma_2(z) \rangle$ at the $\langle 3 \rangle$ wall is evident and particularly the edges of the $\langle 3 \rangle$ wall are affected. Figure 11(d) establishes the presence of a combined order-parameter and composition modulation. The correlated increase of $\langle \sigma_3(z) \rangle + \langle \sigma_4(z) \rangle$ and decrease of $\langle \sigma_1(z) \rangle + \langle \sigma_2(z) \rangle$ is indicative of the order-parameter modulation, while the fact that the decrease of $\langle \sigma_1(z) \rangle + \langle \sigma_2(z) \rangle$ is more significant than the increase of $\langle \sigma_3(z) \rangle + \langle \sigma_4(z) \rangle$ is indicative of the accommodation of excess majority atoms at the $\langle 3 \rangle$ domains. The latter effect is more pronounced at lower temperatures, where the order-parameter modulation becomes less important. The results shown correspond to the following set of interaction parameters: $V_1 = 1$, $V_2 = -0.88$, $V_4 = 0.425$, $V_8 = 0.175$. A more

elaborate report on the MC simulation study will be presented elsewhere in the near future.

6. Phase stability

6.1. Decomposition of the LPS with $M \neq 2$

As pointed out by Iwasaki *et al* (1960) and Iwasaki (1962), the transformation of Au_3Zn (H) into the deformation-modulated R_1 and R_2 phases upon cooling cannot be suppressed by quenching in nearly stoichiometric alloys. They reported that the addition of ternary elements, such as Cu, or deviations of the stoichiometry (towards lower Zn contents) do allow a suppression of this transformation. The authors verified these statements by an analysis of binary alloys containing 19.5, 20.5, 21, 22, 23 and 25 at.% Zn annealed at 250 °C (a second series was treated at 300 °C) for periods ranging from 15 min to 1 month: it was found that after short annealing times the alloys with less than 22 at.% Zn were free from the deformation-modulated R_1 and R_2. Longer annealing of Au–(19.5–20.5) at.% Zn (from 1 week to 1 month) at 300 °C resulted, however, in two-phase mixtures of Au_3Zn (H) with $M = 2$ and the disordered Au-rich solid solution, where the Au_3Zn (H) partly transforms into R_1 and R_2 during the quench to room temperature. This is in agreement with the phase segregation, which is expected from the current phase diagrams (Okamoto and Massalski 1989) and with the resistivity measurements for Au–21 at.% Zn and those reported by Iwasaki *et al* (1960).

The decomposition of the LPS with $M \neq 2$ in a mixture of Zn-rich Au_3Zn (H) ($M = 2$) and an Au-rich disordered solid solution is accompanied by a compositional segregation. Our observations indicate that the migration of fourfold junctions of $\langle 3 \rangle$ walls may play an important role in the segregation process. This is indicated by the observations in figure 12, where a regular front of such fourfold nodes in an Au–20 at.% Zn alloy is visible.

6.2. Discussion of the role of the $\langle 3 \rangle$ walls, ledges and discommensuration nodes in the decomposition of the $\langle 2^k 3 \rangle$ structures

The observed $\langle 2^k 3 \rangle$ structures can be considered as finite-temperature-type structures since the Fujiwara square wave is slightly rounded, which is the graphical description of the fact that the position of the APB interfaces is no longer sharply defined. This is only a formal macroscopic description, however.

On a microscopic scale this manifests itself by the fact that the interfaces become 'rough', i.e. ledges and kinks develop. These ledges and kinks are thermal excitations of the interfaces somewhat similar to *phasons* when the interface is considered as a *soliton*.

Experimentally one finds that only the APB limiting the $\langle 3 \rangle$ bands become diffuse, i.e. acquire ledges and kinks. Why are the $\langle 3 \rangle$ bands favoured sites for ledging?

Purely formally this follows from the construction using the rounded square-wave algorithm. In order to find three 'lattice sites' within a half-wave, the two outer sites must be close to or within the rounded 'leading' and 'trailing' edges of the half-wave, ie. in the region where the construction predicts an ill-defined boundary position (figure 2).

How can this be understood physically? We note that the repulsion ($\sim \exp(-x/L)$) between the APB favours the equidistance of the APB. However, their actual separation

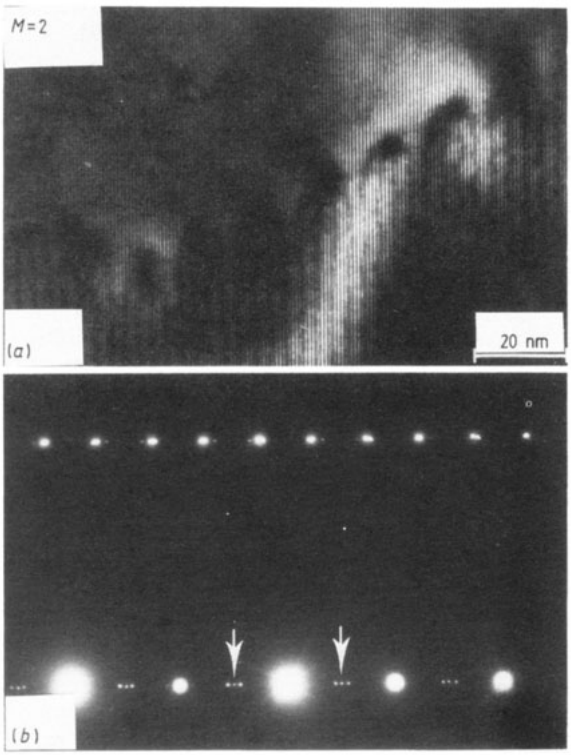

Figure 12. (*a*) Dark-field fringe pattern and (*b*) corresponding electron diffraction pattern for an Au–20 at.% Zn alloy annealed at 300 °C for 4 days. The $M = 2$ structure (upper part in (*a*)) is coexisting with regions where $M \neq 2$ (lower part in (*a*)). The front separating the two phases consists of a regular array of fourfold nodes of ⟨3⟩ domains. Note that the coexistence is also visible in the electron diffraction pattern in (*b*) where the (unsplit) $M = 2$ reflection (indicated by the arrows) is present in between the split satellites corresponding to the region with $M \neq 2$.

pattern is a trade-off between the incommensurate or fractional period imposed by the electronic energy (i.e. the electron/atom ratio or the composition) and the discreteness of the potential sites for the APB, which requires a uniform mixture of two types of blocks, containing an integral number of unit cells. In this sense, the uniform mixtures of ⟨2⟩ and ⟨3⟩ domains observed in Au–Zn alloys are best approximation to a specific constant spacing between 2 and 3.

The possibility of ledging will be largest for those boundaries which are farthest from neighbouring parallel boundaries, since the repulsion is smallest there. Ledging will furthermore take place preferentially towards that side of the boundary on which the separation from the nearest parallel boundary is largest. This is because the ledges or kinks are formed by thermal agitation against the repulsive interaction exerted by the neighbouring APB.

The ledges will thus be easiest to form on the boundaries limiting the ⟨3⟩ bands and in such a way that these boundaries 'meander' in position towards each other, between two locations differing by one lattice parameter. In a sense, the boundary can be thought to be situated in a double well.

Note that, as suggested by the observation in figure 1, one or two of the ⟨3⟩ band boundaries may be affected by ledging. This is in agreement with the predictions of the wave pattern construction (figure 2) and depends on the exact 'phase' of the wave pattern with respect to the site lattice.

It was found experimentally that the elimination of the ⟨3⟩ bands by the formation of fourfold discommensuration nodes causes phase separation to occur; it leaves behind a Zn-enriched ⟨2⟩ structure while it takes away the excess Au and accumulates it in an

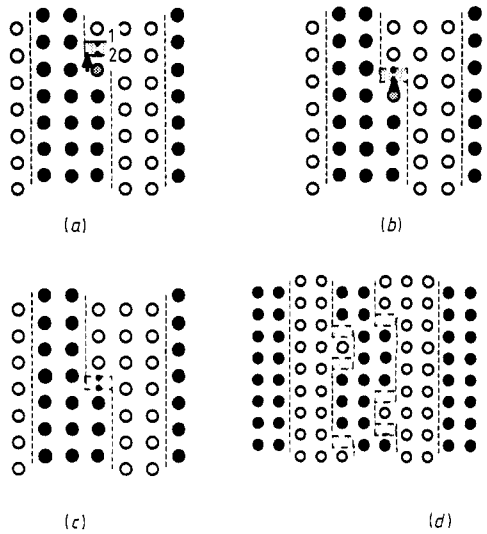

Figure 13. Schematic model drawings relating the presence of ledges (kinks) in the APB limiting the ⟨3⟩ bands to the accommodation and migration of excess Au atoms. (*a*)–(*c*) The downward motion of a ledge causes an upward migration of Zn atoms (arrows) and a sideways motion of the ⟨3⟩ domain. (*d*) Frequent ledges lead to an ill-defined ⟨3⟩ wall position and lead to an averaged model that is a combination of the models in figures 7(*b*) and (*c*).

Au-enriched region, which disorders into the short-range ordered solid solution. This observation sequence seems to suggest that the Zn deficiency is localised at the ⟨3⟩ bands, and particularly at the APB limiting the ⟨3⟩ bands. This suggestion is confirmed by the simulation analysis of the HREM images along both [100] and [110], and the fact that this behaviour is equally encountered in the Monte Carlo simulations for an off-stoichiometric FCC system clearly provides additional support to the model.

A possible model in which the ledges carry with them the excess Au is outlined below. The presence of a ledge or kink in one of the ⟨3⟩ band boundaries, as represented in figure 13(*a*), implies a local deviation from the 3 : 1 composition. The sites marked 1 and 2 in the cross-hatched rectangle could be occupied by a Zn atom in 1 or 2; in both cases a local excess Zn would result. However, since the overall composition is Zn-deficient, it is logical to assume that none of the two sites will be occupied by Zn, but rather by Au. In this manner the non-stoichiometry is partly accommodated by the ledges and kinks in the ⟨3⟩ bands. Figures 13(*b*) and (*c*) indicate how a shift of the ⟨3⟩ band is associated with the interchange of an Au and a Zn atom (upward jump of the Zn atom).

A 'meandering' of the ⟨3⟩ wall boundaries leads to frequent ledges and a significant accommodation of excess Au, since the accommodation is independent of the sign of the ledges. The resulting model, represented in figure 13(*d*), is in fact a microscopic model consistent with the mixture between the 'averaged' models in figures 7(*b*) and (*c*), which was deduced from the analysis of the contrast in the HREM images.

Figure 14 finally represents an instantaneous configuration at a fourfold discommensuration node as corresponding to the HREM image in figure 4. The upward migration of this configuration is equivalent to a downward migration of Zn. The region of $\langle 2^k 3 \rangle$ structure swept by the configuration of discommensurations is thus enriched in Zn so as to leave behind a ⟨2⟩ structure with ideal composition Au_3Zn, as compared to the starting composition $Au_{3+x}Zn$.

6.3. The decomposed microstructures

As discussed in the previous section, the upper part in figure 12(*a*) corresponds to the Au_3Zn (H) with $M = 2$, whereas the migration of the front towards the bottom part

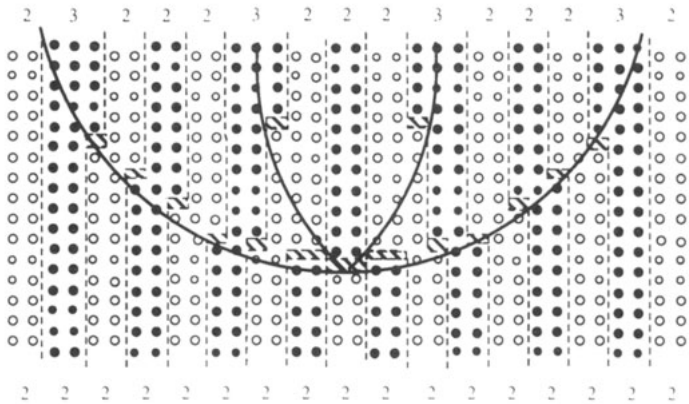

Figure 14. Schematic representation of the projected atom configuration in the vicinity of a discommensuration node. The region of ⟨2ˣ3⟩ structure swept by the configuration of discommensurations is enriched in Zn so as to leave behind a Zn-enriched ⟨2⟩ structure.

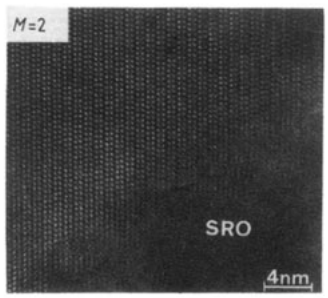

Figure 15. 200 kV [0 1 0] image of an Au–20 at.% Zn alloy annealed at 300 °C for two weeks. Ordered regions with $M = 2$ are dispersed in a disordered matrix (Au solid solution).

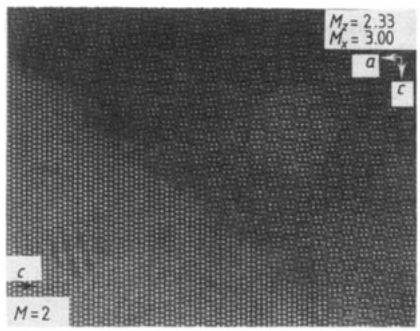

Figure 16. 200 kV [0 1 0] image of an Au–21 at.% Zn alloy annealed at 250 °C for one week. The $M = 2$ structure (lower part) is coexisting with the two-dimensional long-period structure (M_z = 2.33; M_x = 3).

results in the accumulation of the Au excess in a region that has a high density of ⟨3⟩ walls.

When the Au concentration increases, the effective alloy composition in the area moves towards the Au-rich side in the phase diagram until it crosses the order–disorder line and the material disorders. This seems to be the case in figure 15, which corresponds to an Au–20 at.% Zn alloy, which was annealed for two weeks at 300 °C. Ordered regions with $M = 2$ are dispersed in a 'disordered' (short-range ordered) matrix.

Below approximately 285 °C, a two-dimensional long-period structure (2D LPS) is stable for compositions around 17 at.% Zn. Although the kinetics are much slower at, e.g., 250 °C than at 300 or 350 °C, a similar decomposition of the structures with $M \neq 2$ was observed in Au–21 at.% Zn annealed at 250 °C. Fourfold junctions of ⟨3⟩ domains were found to migrate out of the material until they are blocked by twin boundaries (different c axes of the DO_{23}) where they give rise to an accumulation of excess Au,

which allows the nucleation of the 2D LPS on the other side of the twin. A configuration of the coexistence of Au_3Zn (H) and the 2D LPS is shown in figure 16. The lower part corresponds to the Au_3Zn (H) with $M = 2$ whereas the upper part corresponds to the 2D LPS. Note that the modulation of the first type (c axis with $M_z = 2.33$) is in twin relation with the c direction of the 1D LPS with $M = 2$. The second APB modulation ($M_x = 3$) is of the non-conservative type.

It is probably due to the sluggish kinetics that 1D LPS with $M \neq 2$ persist in coexistence with the 2D LPS after annealing of a few weeks at 250 °C in alloys containing 19.5–20.5 at.% Zn. Although the 1D LPS with $M \neq 2$ disappears immediately (in less than 1 h) in alloys containing 22 at.% Zn while they disappear after 1 day annealing in Au–21 at.% Zn, the long persistence for compositions between 19.5 and 20.5 at.% Zn does not allow one to exclude their stability. The rearrangements that are needed for their withdrawal may be inhibited by a well established microstructure, which is formed in order to minimise the strain energy. Earlier studies by Van Tendeloo *et al* (1977) established striking microstructures of coexisting Au_3Zn (H) with $M = 2$ and the 2D LPS in Au–20 at.% Zn alloys, which were treated at 300 °C and afterwards at 250 °C. They referred to this microstructure as a 'checkerboard' pattern.

6.4. The transformation towards the R_1 and R_2 structures

The decomposition of the off-stoichiometric (low Zn content) alloys results in the formation of a two-phase mixture with, as one of its constituents, the Zn-enriched Au_3Zn (H) structure. However, this Au_3Zn (H) is known to transform (partly) to the Au_3Zn (R_1) and (R_2) phases upon cooling. This leads to the observation of these structures in most of the long-time annealed (decomposed) alloys, since all observations are made at room temperature. Figure 17 corresponds to an observation along $[1\,1\,0]_{FCC}$ of an Au–22 at.% Zn alloy, which transformed partly to the room-temperature modification upon quenching. Along this observation direction, no distinction can be made between Au_3Zn (R_1) and Au_3Zn (R_2). The expected images for the Au_3Zn (H) and Au_3Zn (R_2) were computer simulated and compared to the experimental observations in figure 17. The image can be interpreted as partly due to R_2 in the lower part and to Au_3Zn (H) in the upper part: the correspondence with the simulated images for a thickness of 7.2 nm and a defocus of −80 is satisfactory. Microstructures in the single-phase R_2 structure have been investigated by Mäkinen *et al* (1976).

7. Conclusions

A number of sometimes complicated anti-phase domain sequences have been observed, which are in complete agreement with the principle of uniformity. The effects on the images of small changes with respect to the basic model, leading to different models including profile smoothing and composition effects, are analysed by computer simulation and compared with experimental observations.

Additional observations and simulations along the [1 1 0] zone axis, which is less commonly used in the field of long-period structure analysis, strongly support the model in which a fraction of the off-stoichiometry is located at the edges of the ⟨3⟩ walls.

A similar localisation of the excess majority atoms at the ⟨3⟩ walls is evident from the results of Monte Carlo simulations on a 3D FCC Ising model for a non-stoichiometric $\langle 2^k 3 \rangle$ structure, presented here.

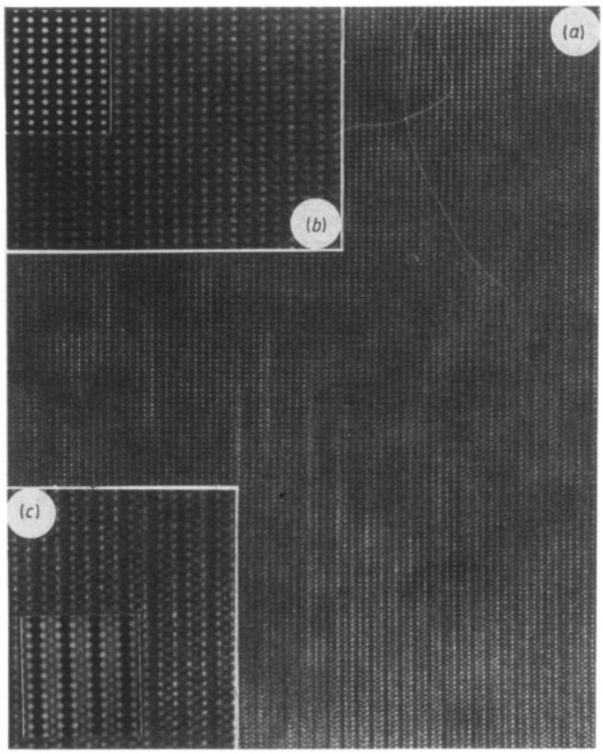

Figure 17. (*a*) 200 kV [1 1 0] image of an Au–22 at.% Zn alloy annealed at 250 °C, which partly transformed to a mixture of AuZn R_1 and R_2 during the quench to room temperature. In (*b*) a part is enlarged which, according to the simulation in the inset, may be interpreted as Au_3Zn (H). The part in (*c*) is in satisfactory agreement with the simulation for the R_2 phase (for the same thickness and defocus as in (*b*): thickness 7.5 nm; $\Delta f = -80$ nm).

Systematic observations after different annealing times clearly indicate that (at least in the 20–22 at.% Zn alloys) the initially present long-period structures with $M \neq 2$ are not stable, since they decompose in a Zn-rich Au_3Zn (H) phase with $M = 2$ and a Zn-poor phase, which can be disordered (above 285 °C) or have a two-dimensional long-period structure (temperatures below 285 °C). (Sluggish kinetics in the alloys with less than 20 at.% Zn do not allow one to draw unambiguous conclusions about the metastability of the structures with $M \neq 2$ at low temperatures (≤ 250 °C).)

It was confirmed that the formation of the distorted R_1 and R_2 phases cannot be suppressed by quenching. Moreover, these phases emerge in all the considered compositions after long enough annealing, since the unstable Zn-rich Au_3Zn (H) phase, which is the precursor of these phases, is obtained after decomposition as one of the end-products.

Acknowledgments

The authors are grateful to J Planes (Office National d'Etudes et de Récherches Aérospatiales, Châtillon, France) for doing the resistivity measurements. We want to thank

M de Graef and L Delaey (Catholic University Leuven, Department of Metallurgy and Materials Engineering) for the long-term use of their thermal annealing facilities. This work has been performed in the framework of the Institute for Materials Science with financial support of the IIKW (Interuniversity Institute for Nuclear Sciences, Brussels).

References

Bak P and von Boehm J 1979 *J. Appl. Phys.* **50** 7409–14
—— 1980 *Phys. Rev.* B **21** 5297
Broddin D, Van Tendeloo G, and Amelinckx S 1988a *EUREM 88 (Inst. Phys. Conf. Ser. 93)* vol 2 (Bristol: Hilger) pp 489–90
—— 1988b *J. Microsc. Spectrosc. Electron.* **13** 40a
Broddin D, Van Tendeloo G, Van Landuyt J, Amelinckx S and De Graef M 1989 *Phil. Mag.* A **59** 979–98
Broddin D, Van Tendeloo G, Van Landuyt J, Amelinckx S and Loiseau A 1988c *Phil. Mag.* B **57** 31–48
Broddin D, Van Tendeloo G, Van Landuyt J, Amelinckx S, Portier R, Guymont M and Loiseau A 1986 *Phil. Mag.* A **54** 395–416
de Fontaine D and Kulik J 1985 *Acta Metall.* **33** 145–65
Fisher M E and Szpilka A M 1987 *Phys. Rev.* B **36** 644–66
Fujiwara K 1957 *J. Phys. Soc. Japan* **12** 7–13
Iwasaki H 1962 *J. Phys. Soc. Japan* **17** 1620–33
Iwasaki H, Hirabayashi M, Fujiwara K, Watanabe D and Ogawa S 1960 *J. Phys. Soc. Japan* **15** 1771–83
Johansson C H and Linde J O 1936 *Ann. Phys., Lpz.* **78S** 439–60
Kulik J, Takeda S and de Fontaine D 1987 *Acta Metall.* **35** 1137–47
Loiseau A, Van Tendeloo G, Portier R and Ducastelle F 1985 *J. Physique* **46** 595–613
Mäkinen K, Paalassalo P and Teuho J 1976 *Ann. Acad. Sci. Fenn.* A **VI 422** 1–10
Okamoto H and Massalski T B 1989 *Bull. Alloy Phase Diagrams* **10** 59–69
Planes J 1988 unpublished work, ONERA, Chatillon, France
Sato H and Toth S 1961 *Phys. Rev.* **124** 1833–47
—— 1962a *J. Phys. Soc. Japan Suppl.* B-II **17** 262–6
—— 1962b *Phys. Rev.* **127** 469–84
—— 1965 *Alloying Behaviour of Concentrated Solid Solutions* ed T B Massalski (New York: Gordon and Breach) pp 295–415
—— 1968 *Bull. Soc. Fr. Minéral. Cristallogr.* **91** 557–74
Schrijvers D, Van Tendeloo G, Van Landuyt J and Amelinckx S 1983 *Phys. Status Solidi* a **75** 607–16
Schubert K, Kiefer B and Wilkens M 1954 *Z. Naturf.* a **9** 987–8
Schubert K, Kiefer B, Wilkens M and Haufler R 1955 *Z. Metallk.* **46** 692–715
Selke W 1988 *Phys. Rep.* **170** (4) 213–64
Terasaki O 1981 *J. Phys. C: Solid State Phys.* **14** L933–8
—— 1982 *J. Phys. Soc. Japan* **51** 2159–67
Terasaki O and Watanabe D 1981 *Japan. J. Appl. Phys.* **20** L381–4
Teuho J 1983 *Phys. Status Solidi* a **80** 589–600
Teuho J, Mäki J and Hiraga K 1987 *Acta Metall.* **35** 721–5
Teuho J and Mäkinen K 1982 *Phys. Status Solidi* a **70** K1–3
Van Dyck D, Danckaert J, Coene W Selderslaghs E, Broddin D, Van Landuyt J and Amelinckx S 1989 *Computer Simulation of Electron Microscope Diffraction and Images* ed W Krakow and M O'Keefe (Providence, RI: American Mathematical Society)
Van Tendeloo G and Amelinckx S 1977 *Phys. Status Solidi* a **43** 553–64
—— 1988 *Phys. Rev.* B **38** 9628–30
Van Tendeloo G, Amelinckx S, Jeng S J and Wayman C M 1986 *J. Mater. Sci.* **21** 4395–402
Van Tendeloo G, Van Landuyt J and Amelinckx S 1977 *Ultramicroscopy* **2** 385–7
Watanabe D and Ogawa S 1956 *J. Phys. Soc. Japan* **11** 226–39
Wilkens M and Schubert K 1958 *Z. Metallk.* **49** 633–46